Magnetic shaping effects on turbulence in ADITYA-U tokamak

OPEN ACCESS
IOP Publishing | International Atomic Energy Agency

Nuclear Fusion

Nucl. Fusion **64** (2024) 106005 (13pp)

https://doi.org/10.1088/1741-4326/ad6b36

Magnetic shaping effects on turbulence in ADITYA-U tokamak

Amit K. Singh[1,2,3,*], **S. Choudhary**[1,2], **M. Gopal Krishna**[1,2], **J. Mahapatra**[1,2], **A. Bokshi**[4], **J. Chowdhury**[1,2], **R. Ganesh**[1,2], **T. Hayward-Schneider**[5], **E. Lanti**[6], **A. Mishchenko**[7], **B.F. McMillan**[8] and **L. Villard**[9]

[1] Institute for Plasma Research, Bhat, Gandhinagar 382428, Gujarat, India
[2] Homi Bhabha National Institute (HBNI), Anushaktinagar, Mumbai 400094, Maharashtra, India
[3] ITER-India, Institute for Plasma Research, Bhat, Gandhinagar 382428, Gujarat, India
[4] York Plasma Institute, Department of Physics, Engineering and Technology, University of York, Heslington, York YO10 5DQ, United Kingdom of Great Britain and Northern Ireland
[5] Max-Planck-Institut für Plasmaphysik, Boltzmannstr. 2, 85748 Garching, Germany
[6] Ecole Polytechnique Fédérale de Lausanne, SCITAS, CH-1015 Lausanne, Switzerland
[7] Max Planck Institute for Plasma Physics, D-17491 Greifswald, Germany
[8] University of Warwick, Coventry CV4 7AL, United Kingdom of Great Britain and Northern Ireland
[9] Ecole Polytechnique Fédérale de Lausanne, Swiss Plasma Center (SPC), CH-1015 Lausanne, Switzerland

E-mail: amitks@ipr.res.in

Received 15 January 2024, revised 5 July 2024
Accepted for publication 4 August 2024
Published 14 August 2024

Abstract
The work reported in this paper addresses two aspects. In the first part, numerical simulations are conducted to examine the impact of magnetic equilibrium shaping (elongation and triangularity), on both conventional Ion Temperature Gradient (ITG) modes and Short Wavelength ITG modes. This analysis is performed considering the experimental profiles and parameters of the ADITYA-U tokamak, employing the nonlinear global gyrokinetic Particle-in-Cell code ORB5. The linear and nonlinear collisionless electrostatic simulation of these modes are carried out with kinetic ions and adiabatic electrons. From the linear results, it has been observed that the magnetic equilibrium shaping slighty reduced the growth rates and widened the spectrum, and the maxima of growth rate curve is shifted to higher toroidal wave number. We find that the heat flux is reduced by a significant $\simeq$35% for the true circular magnetohydrodynamic magnetic equilibrium as compared to ad hoc concentric circular equilibrium reported in Singh *et al* (2023 *Nucl. Fusion* **63** 086029). A further $\simeq$10% reduction in the heat flux is seen with magnetic equilibrium shaping. In the second part, linear collisionless electrostatic simulation studies of ITG coupled with fully kinetic electrons (both trapped and passing electrons are treated kinetically) using a drift-kinetic ordering is performed. It can be seen from the linear results that, in presence of kinetic electrons, the growth rate and real frequency of the ITG mode are increased significantly for ADITYA-U parameters and a mode propagating in the electron diamagnetic direction is identified at high toroidal wavenumbers.

* Author to whom any correspondence should be addressed.

Keywords: global gyrokinetic, ITG, TEM, ADITYA-U, nonlinear simulations, shaped magnetic equilibrium

(Some figures may appear in colour only in the online journal)

1. Introduction

Anomalous transport in tokamaks is believed to be caused by turbulence driven by a variety of micro-instabilities [1–3]. At low plasma beta, these are essentially electrostatic in nature and comprise Ion Temperature Gradient (ITG), Trapped Electron Modes (TEMs) and Electron Temperature Gradient (ETG) modes. The presence of density and temperature variations in a magnetically confined plasma provides the necessary free energy for micro-instabilities. For instance, even at $k_\theta \rho_s > 1.0$, the ITG mode, which is triggered by ITGs, becomes unstable in the presence of extremely sharp background gradients [4, 5]. This instability results in the emergence of short wavelength ITG modes (SWITGs) [4–7]. Gyrokinetic simulations reveal the importance of these short wavelength micro-instabilities for experimental parameters [8]. Therefore, it is vital to understand the linear and nonlinear properties of these modes and their role in the anomalous transport of energy and particles. ADITYA-U [9, 10] is a small-size tokamak ideal for studying micro-instabilities in the presence of sharp density and temperature gradients. Recently reported gyrokinetic simulations [11], which were done using ORB5 [12, 13] with non-adiabatic ions and adiabatic electrons, demonstrate that SWITG mode naturally coexists with the conventional ITG mode in ADITYA-U due to sharp temperature and density gradients. However, in plasmas confined by inhomogeneous magnetic fields, a portion of electrons become trapped in low magnetic field regions. These trapped electrons can either intensify micro-instabilities derived from ion dynamics, such as the ITG-TE (ITG coupled with trapped electron) mode, or generate other forms of instabilities known as trapped particle mode [2, 3, 14–18]. Likewise, the presence of significant gradients can also lead to a shorter wavelength branch of TEMs [19, 20].

Further, the ADITYA-U tokamak is planned to have a controlled shaped plasma operation, the impact of which on ITG-SWITG branch could be substantial. Studies conducted through numerical simulations utilizing local δf gyrokinetic (GK) codes and analytical equilibrium models have demonstrated that larger elongations and higher triangularity (at high elongations) have a stabilizing impact on ITG-ae (ITG with adiabatic electron) and ITG-TEs [21, 22]. It has also been observed using global codes [23, 24], higher elongations provide a stabilizing effect. The significance of plasma shaping effects, including elongation, triangularity, and Shafranov shift, in enhancing tokamak performance has been recognized for a considerable time. It is understood that these shaping effects can control the growth rate of ITG turbulence, and the level of ITG turbulence can also be regulated by zonal flow (ZF). Furthermore, recent numerical simulations indicate that the shaping effects can have an impact on the level of collisionless residual ZF [21, 22, 25, 26].

Following the work reported in [11] which was performed with an ad hoc concentric circular equilibrium and treated the electrons adiabatically, the present work extends this to both shaped magnetohydrodynamic (MHD) equilibria and a kinetic electron treatment. The manuscript is structured as follows: section 2 describes the numerical model used in simulation along with the numerical setup. In section 3 the effect of magnetic equilibrium shaping (elongation and triangularity) on ITG and SWITG modes is assessed through linear and nonlinear global GK simulations with kinetic ions and adiabatic electrons. In section 4 we present our linear findings from treating the electrons kinetically while remaining electrostatic and collisionless. Finally, conclusions are drawn in section 5.

2. ORB5 gyrokinetic model

In the ORB5 code, the Vlasov-Poisson system is solved in the gyrokinetic limit for an axisymmetric toroidal plasma. The radial coordinate is defined as $s = \sqrt{\psi/\psi_{\text{edge}}}$, where ψ is the poloidal flux. Circular concentric magnetic surfaces, representing ad hoc equilibrium [27], and true MHD equilibrium are distinct types of magnetic equilibria incorporated into the ORB5. In the case of true MHD equilibrium, the Grad–Shafranov equation is solved with a fixed plasma boundary using the CHEASE code [28], and subsequently, it is coupled with the ORB5 code. It's noteworthy that ORB5 employs a straight field line coordinate system. Under gyrokinetic framework, the time evolution of ion distribution function is given by:

$$\frac{\partial f_i}{\partial t} + \dot{\mathbf{X}} \cdot \nabla f_i + \dot{v_\parallel} \frac{\partial f_i}{\partial v_\parallel} = C + S \tag{1}$$

where $\mathbf{X}$ is the position of gyro-center in real space, $v_\parallel$ is the component of velocity parallel to the equilibrium magnetic field $\mathbf{B} = B\mathbf{b}$, here C and S indicates collisions and sources respectively. Though ORB5 is both fully electromagnetic [29] and collisional [30] code, this work addresses the electrostatic and collisionless limits. For a species with charge q and mass m, the equations of motion are given by,

$$\dot{\mathbf{X}} = v_\parallel \mathbf{b} + \frac{B}{B_\parallel^\star} \left(\mathbf{v}_{\nabla \mathbf{B}} + \mathbf{v}_{\mathbf{E}\times\mathbf{B}} + \mathbf{v}_\mathbf{c}\right), \tag{2}$$

$$\dot{v_\parallel} = -\left(\frac{1}{m}\mathbf{b} + \frac{1}{m v_\parallel} \frac{B}{B_\parallel^\star} \left(\mathbf{v}_{\nabla \mathbf{B}} + \mathbf{v}_{\mathbf{E}\times\mathbf{B}} + \mathbf{v}_\mathbf{c}\right)\right) \cdot \left(\mu \nabla B + q \nabla \langle\phi\rangle_G\right), \tag{3}$$

where $\mathbf{v}_{\nabla \mathbf{B}} = (\mu/(m\Omega B))\,\mathbf{B} \times \nabla B$ represents the grad-B drift velocity, $\mathbf{v}_{\mathbf{E}\times\mathbf{B}} = (1/B^2)\,\mathbf{B} \times \nabla \langle\phi\rangle_G$ represents the $\mathbf{E} \times \mathbf{B}$ drift velocity, and $\mathbf{v}_\mathbf{c} = (v_\parallel^2/\Omega)\,(\nabla \times \mathbf{b})_\perp$ denotes the curvature drift velocity. Here, the gyroaveraged electrostatic potential is denoted by $\langle\phi\rangle_G$. Finally, the effective magnetic field ($\mathbf{B}^\star$) is written as

$$\mathbf{B}^\star = \mathbf{B} + \frac{B}{\Omega} v_\parallel \nabla\times\mathbf{b} = B_\parallel^\star \mathbf{b} + \frac{B}{\Omega} v_\parallel (\nabla\times\mathbf{b})_\perp = B_\parallel^\star \mathbf{b} + \frac{B}{v_\parallel}\mathbf{v_c} \tag{4}$$

The closure of the system of equations (1)–(3) is accomplished through the incorporation of the gyrokinetic Poisson equation under the assumption of quasi-neutrality.

$$\sum_\alpha q_\alpha \delta n_\alpha = 0 \tag{5}$$

where, δn_α represents the perturbed density, with the summation encompassing all plasma species denoted by α. Equation (5) undergoes a transformation, evolving into a linear integral equation governing the electrostatic potential, as expressed by equation (6).

$$\frac{q_i}{m_i}\nabla_\perp\cdot\frac{n_{0i}}{\Omega_{0i}^2}\nabla_\perp\phi - \frac{q_e n_{0e}}{T_{0e}}\left(\phi - \langle\phi\rangle_{FS}\right) = \delta\bar{n}_i \tag{6}$$

In equation (6), $\langle\phi\rangle_{FS}$ represents a flux-surface-averaged electric potential. More details of model equations can be found in [12, 13]. All quantities in the code are normalized using four parameters: the ion mass (m_i), the ion charge ($q_i = Z_i e$, where Z_i is the atomic number and e is the electric charge), the electron temperature at a specified reference position s_0 ($T_e(s_0)$), and the magnetic field on axis (B_0). These parameters serve to determine all other normalized quantities. Time units are defined as the inverse of the ion-cyclotron frequency, $\Omega_{ci} = q_i B_0/m_i$. Velocity units are normalized using the ion sound velocity ($c_s = \sqrt{eT_e(s_0)/m_i}$, with $T_e(s_0)$ in electron volts), length units are normalized via the ion sound Larmor radius ($\rho_s = c_s/\Omega_{ci}$).

3. Effects of magnetic equilibrium shaping on ITG-SWITG modes

The recently upgraded ADITYA-U tokamak [9, 10] is a medium aspect ratio tokamak with divertor configuration [10]. It is well suited to study microinstabilities in the presence of temperature and density gradients. In this section, we extend the work in [11, 31] to include the effect of magnetic equilibrium shaping. The simulations are conducted on spatial grids $N_s = 448, N_{\theta_\star} = 512, N_\varphi = 256$, $(s, \theta_\star, \varphi)$ representing the radial, poloidal, and toroidal directions.

The number of markers is $N_p = 100\times10^6$, the time step is $\Delta t = 10\Omega_{ci}^{-1}$ and $\rho_* = \rho_s/a = 0.00365$. The ITG instability is taken at the peak ($s_0 = 0.6$) of the temperature and density gradients. In the density and temperature profiles, the symbols δ_{s_n} and δ_{s_T} represent the radial width of the density and temperature profiles, respectively. L_n and L_T denote the density and temperature gradient scale lengths, respectively. Each linear simulation corresponds to a single toroidal mode number. The profiles and parameters that are used in the simulation of ADITYA-U are depicted in table 1 and figures 1(*a*)–(*c*). Three distinct MHD equilibria have been investigated in this paper: (i) a circular equilibrium with $\kappa = 1.0$, motivated by the experimental shot studied in [11]; (ii) a shaped equilibrium with $\kappa = 1.2, \delta = 0.45$ reported by [9]; and (iii) an equilibrium with $\kappa = 1.4, \delta = 0.45$, which is the theoretical maximum elongation (and triangularity) that is achievable on ADITYA-U with the current vacuum vessel.

3.1. Linear gyrokinetic simulations

In this subsection, we present the linear gyrokinetic simulations of ITG-SWITG modes for circular and shaped magnetic equilibria. The growth rates and real frequencies are calculated using ORB5 for different toroidal mode numbers and are shown in figures 2(*a*) and (*b*) respectively. As depicted in figure 2(*a*), the growth rate exhibits two peaks instead of the typical single peak observed in linear standard ITG modes. The second peak is the characteristic of the SWITG mode. In this toroidal mode numbers n scan, elongation (κ) takes values of 1.0 (MHD circular equilibrium), 1.2 (shaped MHD equilibrium) and 1.4 (shaped MHD equilibrium). All the magnetic equilibria are obtained from CHEASE code [28]. Both shaped cases have the same triangularity value of $\delta = 0.45$.

The frequency of ITG-SWITG in figure 2(*b*) shows a non monotonous behavior. This can be explained as follows. The poloidal mode number ($k_\theta\rho_s$) is computed using the relationship $k_\theta\rho_s = \frac{nq\rho_s}{r}$. In the figure 2, the toroidal mode numbers are scanned in the range of $0-160$ corresponding to the poloidal wavenumbers ($k_\theta\rho_s = 0-2.0$). For $k_\theta\rho_s \leqslant 1$, the real frequency increases monotonically with $k_\theta\rho_s$, but then almost stays constant for $1 \leqslant k_\theta\rho_s \leqslant 2.0$. The following dispersion relation for SWITG [32, 33] for adiabatic electrons is obtained by the quasi-neutrality equation in the context of a local gyrokinetic formulation in the limit $\omega_{*i} > \omega > (\omega_{di} + k_\parallel v_\parallel)$, where ω_{di} is the ion magnetic drift frequency. The dispersion relation for the SWITG mode is given as, $\omega = \frac{\tau}{\tau+1}\left(\frac{\eta_i}{2}-1\right)\omega_{*i} I_0(k_\theta^2\rho_s^2)\exp(-k_\theta^2\rho_s^2)$. Here, $\tau = T_e/T_i$, I_0 is the modified Bessel function of order zero, $\omega_{*i} = -(v_{thi}/L_n)(k_\theta\rho_s)$ is the ion diamagnetic drift frequency, and L_n is the density scale length. It can be seen from the expression of the dispersion relation, that the mode frequency ω scales as $k_\theta\rho_s$ for small $k_\theta^2\rho_s^2$ and for larger $k_\theta^2\rho_s^2$ ($k_\theta\rho_s \gg 1$) scales almost as constant as $I_0(k_\theta^2\rho_s^2)\exp(-k_\theta^2\rho_s^2) \rightarrow 1/\sqrt{2\pi(k_\theta^2\rho_s^2)} = 1/(\sqrt{2\pi}k_\theta\rho_s)$.

It can be seen from the figure 2(*a*) that the maximum linear growth rates for the both modes (ITG and SWITG) are a little reduced with magnetic equilibrium shaping and the spectrum is widened with the maximum growth rate shifted to higher toroidal wave number (n). This similar type of observation was reported in [25] for the conventional ITG modes. It can also be seen from figure 2(*b*) that the real frequencies are decreasing with magnetic equilibrium shaping. It has also been reported in [25] that the global ITG mode sees an average temperature gradient, and the scale length of the temperature gradient is modified to $R(1-E')/L_T$ with $E' = r(\kappa-1)/(\kappa+1)$, where r is the magnetic surface label coordinate. Therefore, the scale length of temperature gradient is reduced with magnetic equilibrium shaping. As we see that the driving source for ITG is reduced therefore both the growth

Table 1. Parameters and equilibrium profiles of ADITYA-U.

Parameters:	Equilibrium Profiles:
• B-field : $B_0 = 1.0$ Tesla, $\frac{m_i}{m_e} = 1836$	• **N-profile and T-profile:**
• Density: $N_0 = N(s_0) = 0.955 \times 10^{19}$	$N(s)/N_0 = \exp(-\frac{a\,\delta s_n}{L_n}\ \tanh(\frac{s-s_0}{\delta s_n}))$
• Temperature : $T_0 = T(s_0) = 78$ eV	$T_{i,e}(s)/T_0 = \exp(-\frac{a\,\delta s_T}{L_T}\ \tanh(\frac{s-s_0}{\delta s_T}))$
• Major radius : $R_0 = 0.75$ m	$\delta s_n = 0.665,\ \delta s_T = 0.13$ at $s = s_0$
• Minor radius : $a = 0.25$ m	• ***q*-profile and $\hat{s}$-profile:**
• Radial coordinate : $s,\ s_0 = 0.6$	$q(s) = 1.25 + 0.67\, s^2 + 2.38\, s^3 - 0.06\, s^4$
•$L_n = 0.136\, m,\ L_T = 0.028$	such that $q(s = s_0) = 2.0$;
$m \rightarrow \eta_{i,e}(s_0) = L_n/L_T = 4.86$	
•$\tau(s) = T_e(s)/T_i(s) = 1$,	shear $\hat{s}$ is positive and at $s = s_0,\ \hat{s} = 1$.
$\epsilon_n = L_n/R_0 = 0.18$,	
$\epsilon_T = L_T/R_0 = 0.037$.	

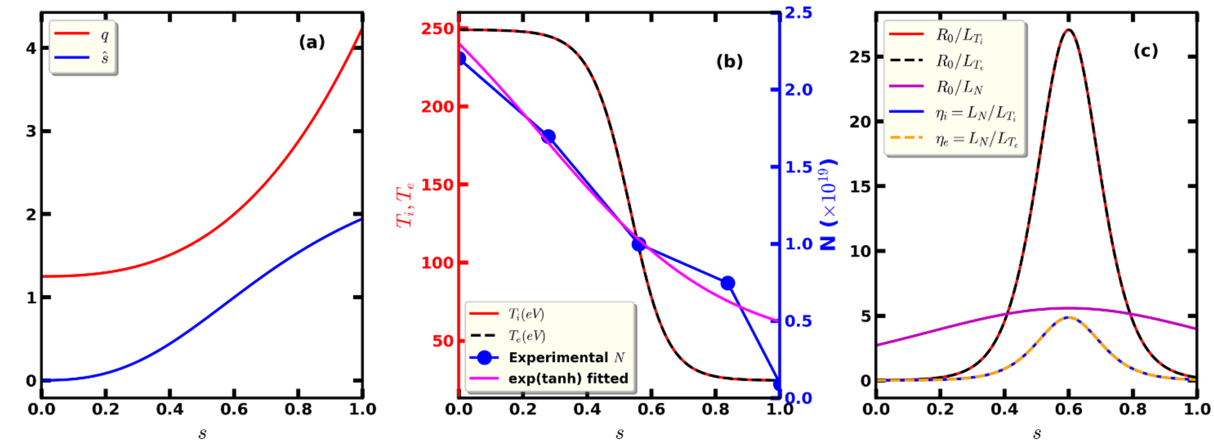

Figure 1. Equilibrium profiles of ADITYA-U taken from [11] (*a*) safety factor (q) & shear ($\hat{s}$) profiles (*b*) T_i and T_e are the ion and electron temperature profiles respectively and N is the experimental and fitted density profiles (*c*) $R_0/L_{T_{i,e}}$ & R_0/L_N are the normalized temperatures and density scale lengths and $\eta_{i,e} = L_N/L_{T_{i,e}}$.

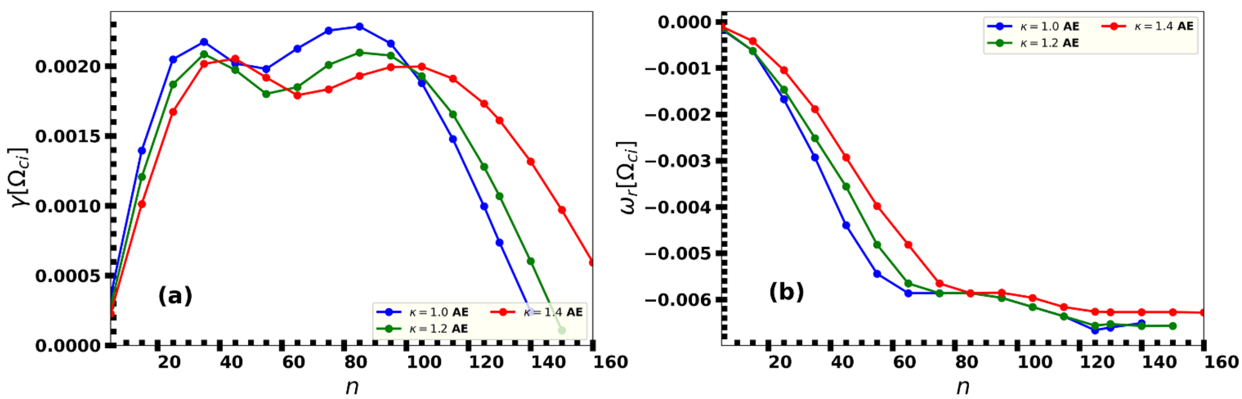

Figure 2. (*a*) Growth rate (γ/Ω_{ci}) and (*b*) frequency (ω_r/Ω_{ci}) as a function of the toroidal mode number n for circular (blue), $\kappa = 1.2, \delta = 0.45$ (green) and $\kappa = 1.4, \delta = 0.45$ (red) MHD equilibria.

rate and real frequencies are decreased. Therefore elongation plays an important role to stabilize the ITG as well as SWITG modes. Figures 3(*a*) and (*b*) show the 2D poloidal mode structure for circular equilibrium obtained from ORB5 for toroidal wave numbers $n = 35$ and $n = 85$, respectively. The corresponding poloidal wave numbers are $k_\theta \rho_s \simeq 0.4$ (first peak) and $k_\theta \rho_s \simeq 1.2$ (second peak), respectively. The mode structures for shaped MHD equilibrium ($\kappa = 1.4$) for toroidal mode numbers $n = 45$ (first peak) and $n = 95$ (second peak), respectively, are also shown in figures 3(*c*) and (*d*) respectively.

Following the linear simulation, in the below subsection we present the magnetic equilibrium shaping effects on ITG-SWITG modes with adiabatic electrons through nonlinear global simulations.

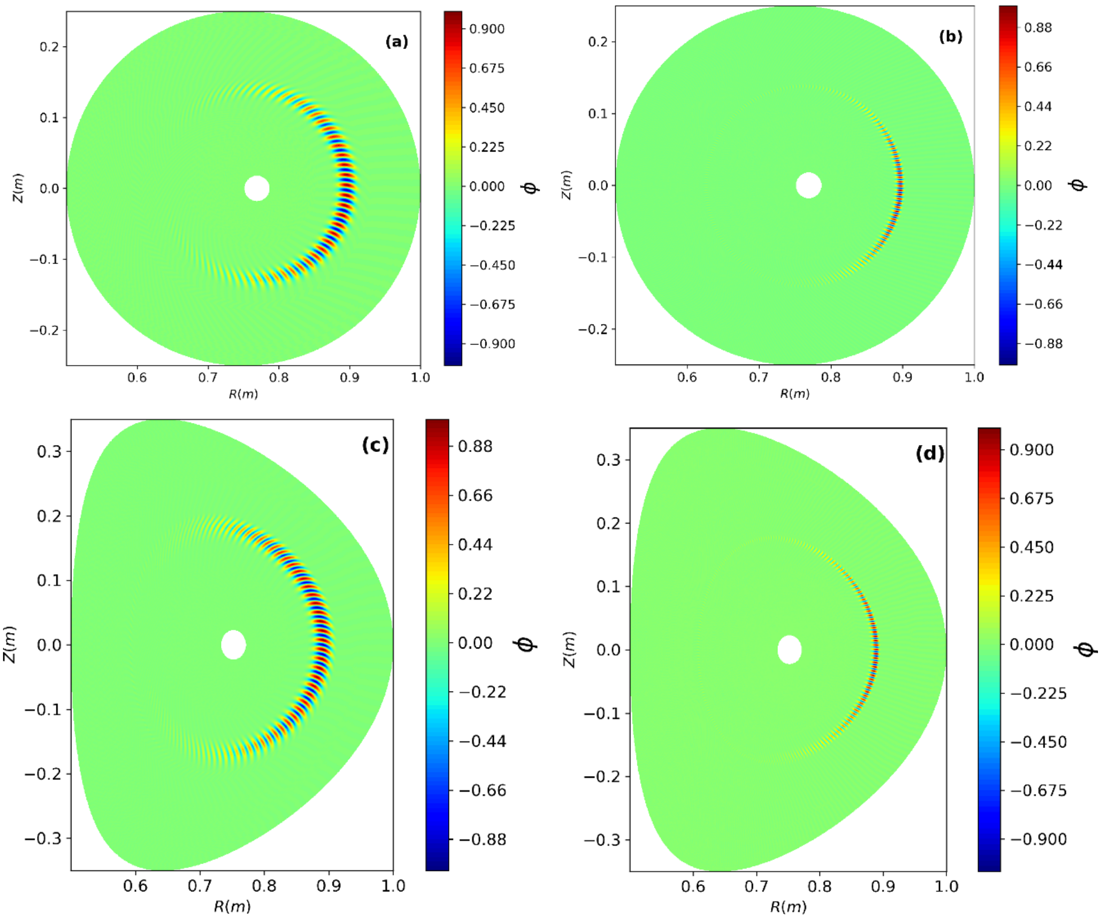

Figure 3. Top panel shows the 2D poloidal mode structure for the (*a*) $n = 35$ and (*b*) $n = 85$ instability from the circular equilibrium, whereas the bottom panel shows the (*c*) $n = 45$ and (*d*) $n = 95$ modes for the shaped ($\kappa = 1.4$) equilibrium. Each n corresponds to the respective ITG and SWITG peak growth rates.

3.2. Nonlinear gyrokinetic simulations

In this subsection, we will outline our findings for effect of magnetic equilibrium shaping on the nonlinear simulation of ITG-SWITG modes with adiabatic electrons. The number of markers is $N_p = 200 \times 10^6$. The 3D grid resolution for the fields solver is $N_s \times N_{\theta_\star} \times N_\varphi = 448 \times 1024 \times 512$. A field-aligned Fourier filter is applied with $n_{\max} = 125$ ($n_{\max}$ is the maximum value of the toroidal mode number), which keeps only the modes almost aligned with the background magnetic field, i.e. $m \in [nq - \Delta m, nq + \Delta m]$, for all $n \in [0, n_{\max}]$ where (m, n) are the poloidal and toroidal mode numbers, respectively, and Δm is the width of the field-aligned filter. Adaptive technique is employed for the gyro-averaging with maximum 64 gyro-points. The arbitrary wavelength field solver [34–36] is used for the quasi-neutrality equation and the time step size is $\Delta t = 10\Omega_{ci}^{-1}$. Convergence test for the grid resolution and time steps for nonlinear simulation have already been conducted and reported in [11]. The simulation includes toroidal mode numbers n ranging from 0 to 125 and poloidal mode numbers m spanning from -270 to 270. This range corresponds to poloidal wave numbers $k_\theta \rho_s$ covering values from 0.0 to 1.4. All the simulations have a sufficiently high signal-to-noise ratio, $S/N > 30$. As indicated in equation (1), S stands for the sources that can be added to regulate numerical noise and/or maintain temperature and density profiles; $S = S_k + S_h$, where S_h is a heating source term (considered zero in the present simulation) and S_k is a Krook operator [37]. The Krook operator, $S_k = -\gamma_K \delta f + S_{\text{corr}}$, where $\gamma_K \sim \gamma_{\max}/10$, with $\gamma_{\max}$, the maximum linear growth rate. A correction term, S_{corr} is designed to conserve the particle density, the parallel momentum, the kinetic energy, and the ZFs [37]. In the present simulation, we used 'gradient-driven' simulations using Krook operator to maintain the profiles gradient [11, 38–40] such as to conserve, the density, parallel momentum, and ZF residual phase space structures. This operator permits a certain level of relaxation of the temperature profiles [11, 37, 40]. Boundary condition for the electrostatic potential is the unicity [34, 41] at the magnetic axis, $\delta\phi(s = 0, \theta^*) = \langle \delta\phi \rangle_\theta (s = 0)$, for all θ^* and at the plasma boundary ($s = 1$), it obeys natural boundary conditions described in [34]. When numerical particles (markers) leave the plasma, they are placed back into the plasma with a zero weight ($\delta f = 0$ is set to zero along characteristics of the Vlasov equation which cross the boundary with negative radial velocity) conserving their energy, magnetic moment, and toroidal canonical momentum [39].

The ambient plasma profiles defining f_0 are fixed. The 'mean-field' ZF is extracted from the fluctuating electrostatic potential. It is not evolved separately from the electrostatic potential.

The normalized electrostatic field energy and normalized volume-averaged heat flux are depicted in figures 4(*a*) and (*b*) for circular, $\kappa = 1.2$ and $\kappa = 1.4$ respectively. For all the cases in figure 4(*a*), the electrostatic field energy exhibits an initial phase of exponential growth over time, followed by a subsequent nonlinear saturation phase. The electrostatic field energy E_{field}, defined as [12]

$$E_{\text{field}} = \int \frac{q_i}{2} \left(\langle n_i \rangle_G - n_0 \right) \phi \, \mathrm{d}\vec{R} \tag{7}$$

where $\langle \quad \rangle_G$ denotes a gyro-averaged quantity and n_0 is the equilibrium density. From figure 4(*a*), it can be observed that after the initial linear phase the mode amplitude gradually saturates from time $t \sim 25.0 \times 10^3 \Omega_{ci}^{-1}$, for all the cases. The normalized field energy is given as $E_{\text{field}}/(\langle n \rangle V T_e)$, where V is the plasma volume, n is the density and $\langle n \rangle$ its averaged value in space and $T_e = T_e(s_0)$ is the electron temperature at $s_0 = 0.6$. Figure 4(*b*) and displays the volume-averaged heat flux Q for circular and shaped equilibrium ($\kappa = 1.2$ & $\kappa = 1.4$) respectively, defined by [12]

$$Q = \frac{1}{V} \int_V \mathrm{d}\vec{R} \int f\left(\vec{R}, v_\parallel, \mu, t\right) \frac{1}{2} m_i v^2 \frac{\langle \vec{E} \rangle_G \times \vec{B}}{B B_\parallel^*} \cdot \frac{\nabla \psi}{|\nabla \psi|} B_\parallel^* \mathrm{d}v_\parallel \mathrm{d}\mu \tag{8}$$

and the normalized heat flux is given as $Q/(\langle n \rangle c_s T_e(s_0))$.As depicted in figure 4(*b*), the heat flux undergoes an initial exponential rise during the linear phase, reaching its peak around $t \sim 1.5 \times 10^4 \Omega_{ci}^{-1}$. Subsequently, with the progression of time, the simulation transitions into the nonlinear phase approximately at $t = 2.5 \times 10^4 \Omega_{ci}^{-1}$, where the ZF sets in. There is an overall reduction in heat flux and tends towards the steady state due to interaction between turbulence and ZF. The time-averaged heat flux in the steady state is around 0.0234 in the normalized unit for circular case while it is 0.021 for the shaped MHD equilibrium ($\kappa = 1.4$). The heat flux is slightly reduced by $\simeq 10\%$ due to magnetic equilibrium shaping as compared to circular equilibrium. The heat flux is found to be reduced by a significant $\simeq 35\%$ for true circular MHD magnetic equilibrium as compared to ad hoc concentric circular equilibrium. The heat flux in ADITYA-U with ad hoc concentric circular equilibrium is reported in [11]. The observed differences ($\simeq 35\%$) in the heat flux mainly appears to come from the nonlinear simulations between the two equilibrium models. The differences in the heat flux may be attributed to the presence of the Shafranov shift, characterized by the horizontal displacement of flux surface centers with respect to the magnetic axis. As is well known, this shift arises from forces exerted by kinetic and magnetic pressures. Notably, the ad-hoc concentric circular equilibrium model assumes a zero Shafranov shift [27], whereas in the real MHD equilibrium, the Shafranov shift naturally arises through the Grad-Shafranov solver. The study reported in [42, 43] indicates that an increase in the Shafranov shift contributes to the stabilization of the ITG mode. We therefore emphasize that, where possible, gyrokinetic simulations should employ a proper treatment of the equilibrium.

From figure 4(*a*), we see that the electrostatic field energy decreases due to magnetic shaping (elongation) effects. This effects can be explained by figure 5. From figure 5, we see that both the amplitude and the spectral distribution of the electrostatic potential are affected (turbulence is lower in the shaped plasma, with the energy spectrum slightly shifted towards smaller scales). The reduction of the electrostatic field energy can also be explained from the linear simulation. As, we can from figure 2(*a*), linear growth rates of ITG-SWITG modes are decreased due to magnetic shaping effects.

Figure 6 shows the spatio-temporal behavior of the turbulent energy (non-zonal component of the electrostatic field energy) for circular and shaped cases. The mode intensity peaks at time $t \sim 1.5 \times 10^4 \Omega_{ci}^{-1}$ and around $s = 0.65$. The turbulence exists over a wide radial domain approximately from $s = 0.5$ to $s = 0.8$. Radial plot of $\eta = L_n/L_T$ for both cases is also shown in figures 6(*a*) and (*b*), respectively, at three time points at (1) the start (orange dashed line) (2) intermediate (white dashed line) and (3) end of the simulation (green dashed line). From figures 6(*a*) and (*b*), we can see that the turbulent energy has its maximum amplitude pushed a bit outwards from the position of maximum log gradient. It looks much more active in the interval $s \in [0.55 - 0.75]$ for both the cases (circular and shaped).

Plots of the electrostatic turbulent potential $\tilde{\phi} = \phi - \langle \phi \rangle_{FS}$ at $t = 2.0 \times 10^5 \Omega_{ci}^{-1}$, (where $\langle \phi \rangle_{FS}$ is the flux surface averaged potential) during the nonlinear simulations for circular and shaped magnetic equilibrium ($\kappa = 1.4$) are shown in figures 7(*a*) and (*b*) respectively. $E \times B$ ZF is widely recognized for its crucial role in regulating turbulence and improving confinement in fusion plasmas [44, 45]. Due to magnetic equilibrium shaping effects, the collisionless residual ZF level can be influenced as reported in recent numerical simulations [21, 22, 25, 26]. The plasma shaping effects on the collisionless residual ZF are also evaluated by an analytical approach which shows that the residual ZF level increases with elongation and triangularity [46]. As we can see from figures 7(*a*) and (*b*), the ZF shear tears the global structures to regulate the turbulence for both the cases. Hence, it is crucial to thoroughly examine the impact of the ZF shearing rate in both cases. The $E \times B$ ZF shearing rate is given by equation (9) [38],

$$\omega_{E\times B}(s,t) = \frac{s}{2\psi_{s0} q} \frac{\partial}{\partial s} \left(\frac{1}{s} \frac{\partial \langle \phi \rangle_{FS}}{\partial s} \right) \tag{9}$$

The shearing rate's temporal evolution is depicted in figures 8(*a*) and (*b*) in both situations. The time and radially averaged shearing rate $\omega_{E\times B}^{\text{tot}} = \langle \langle |\omega_{E\times B}| \rangle_s \rangle_t$ is $0.004\,68 \Omega_{ci}$ for circular equilibrium and $0.004\,79 \Omega_{ci}$ for shaped MHD equilibrium ($\kappa = 1.4$), respectively, are shown with black dashed line in figures 8(*a*) and (*b*), respectively. The subscripts s and t indicate averages over radius ($s \in [0.5 \;\; 0.8]$) and time ($t[\Omega_{ci}^{-1}] \in [1.0 \times 10^5 \;\; 2.0 \times 10^5]$), respectively. The quantity

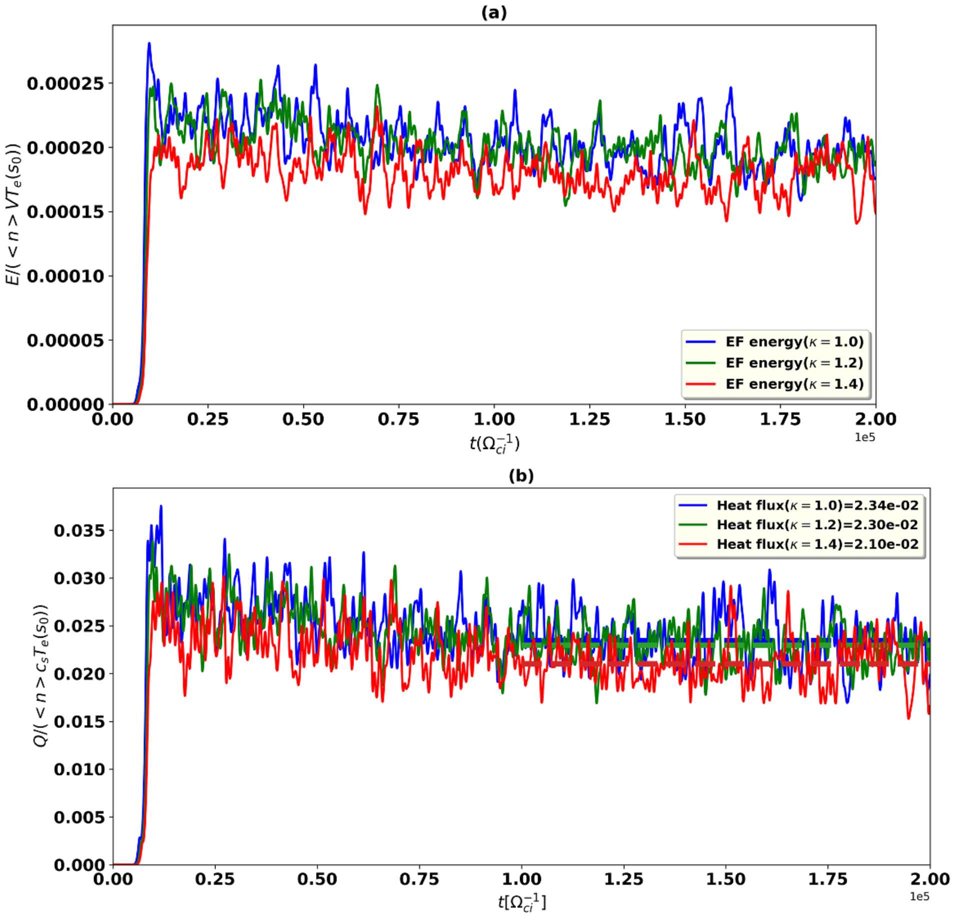

Figure 4. (*a*) Electrostatic field energy and (*b*) Heat flux as a function of time t(Ω_{ci}^{-1}) for the three MHD equilibria under study. The mean heat flux value, averaged over a suitable time window (dashed line), is shown in the label.

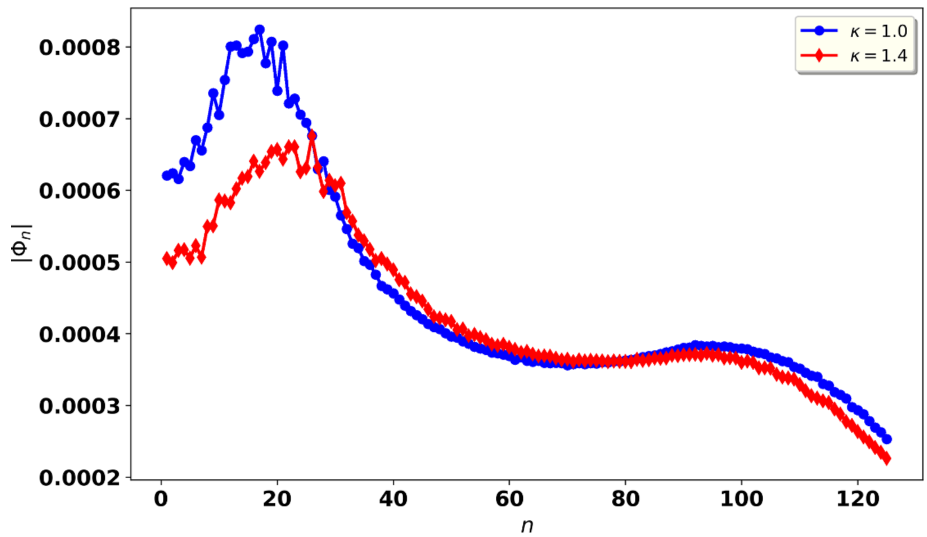

Figure 5. Spectral distribution of the electrostatic potential is plotted in the time averaged interval $t[\Omega_{ci}^{-1}] \in [1.0 \times 10^5 - 2.0 \times 10^5]$ among different toroidal mode numbers n for both circular and shaped ($\kappa = 1.4$) cases for the nonlinear phase of the ITG-SWITG turbulence simulation.

$\omega_{E\times B}^{tot}$ is a measure of the total absolute value of the ZF shearing rate. In the case of circular equilibrium, the ZF shearing rate for the ITG-SWITG mode is slightly less as compared to shaped MHD equilibrium ($\kappa = 1.4$). The dominant process for saturating turbulence associated with the ITG-SWITG mode involves ZFs, as evidenced by the observation that the shearing rate surpasses the linear growth rate in both cases. In order to compare the global mode structure as shown in

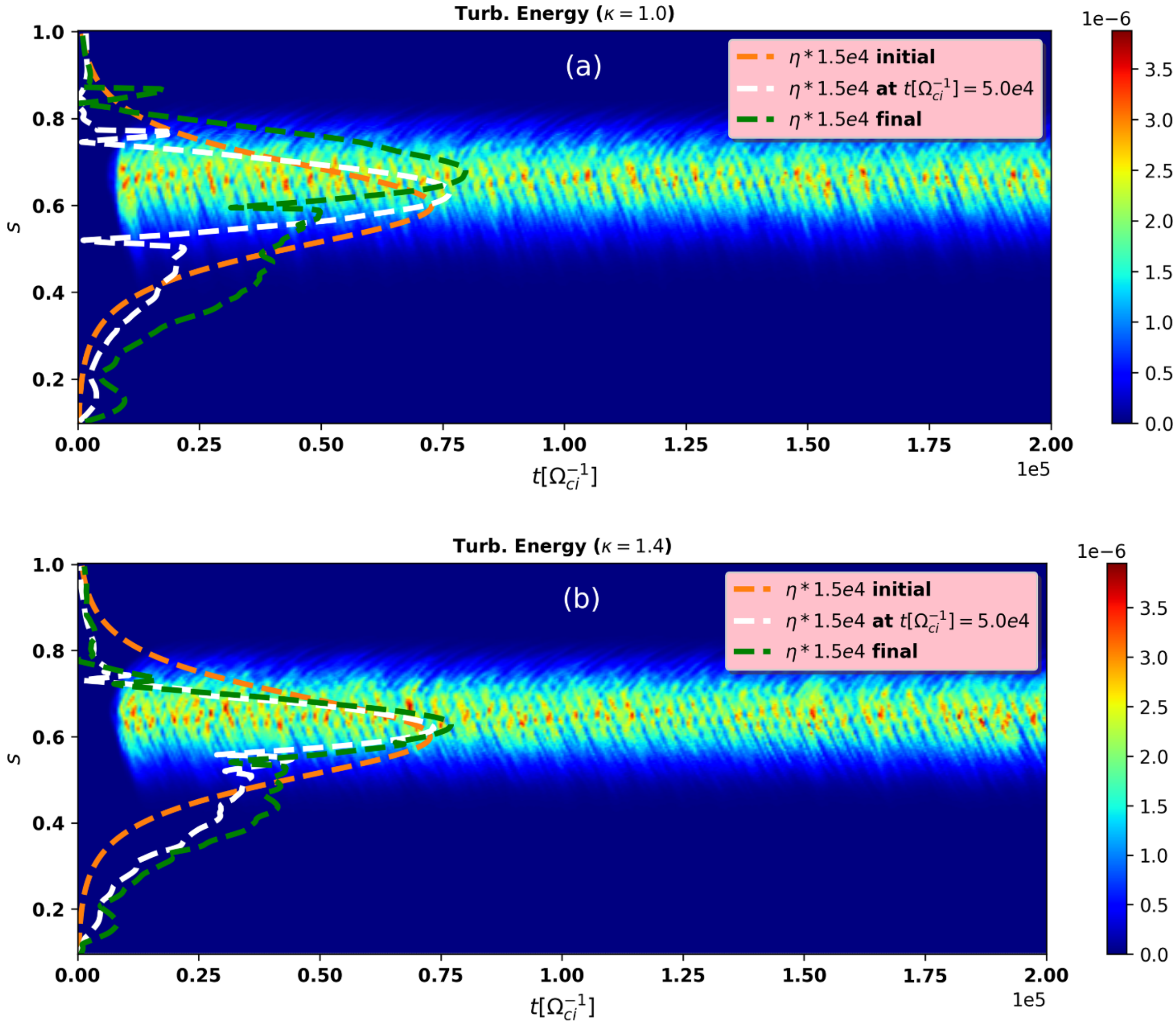

Figure 6. Spatio-temporal contour plots of the turbulent energy (non-zonal component of electrostatic field energy), separately for the circular (top panel) and shaped ($\kappa = 1.4$)(bottom panel) cases. Also shown are the radial plot of $\eta = L_n/L_T$ at initial (orange dashed line), at $t[\Omega_{ci}^{-1}] = 5.0 \times 10^4$ (white dashed line) and final (green dashed line) times. The factor 1.5×10^4 is multiplied in the η profile for visibility.

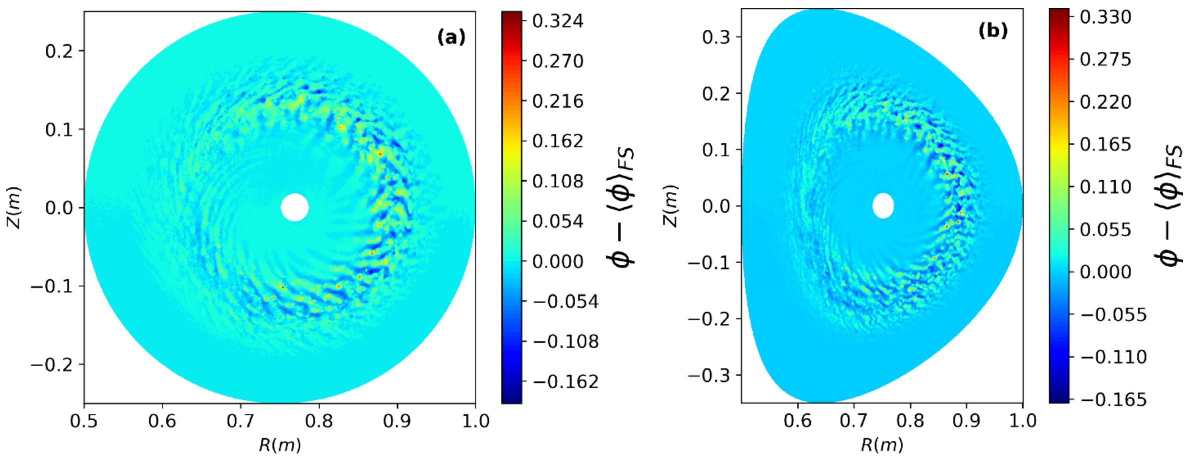

Figure 7. 2D poloidal mode structure of the turbulence for the (*a*) circular and (*b*) $\kappa = 1.4$ equilibrium at the final time point in simulations.

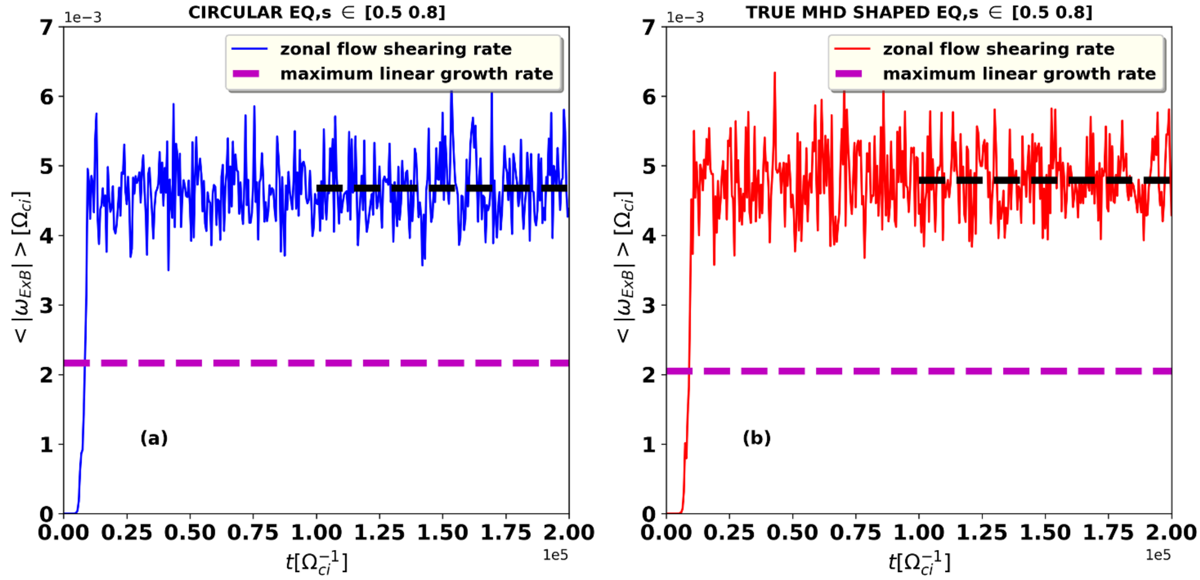

Figure 8. The time history of the $E \times B$ zonal flow shearing rate ($\omega_{E\times B}$) for (*a*) circular and (*b*) $\kappa = 1.4$. The magenta dashed lines depict the corresponding maximum linear growth rates for the ITG mode, i.e. $0.002\,17\Omega_{ci}$ and $0.002\,05\Omega_{ci}$, respectively.

figures 7(*a*) and (*b*) quantitatively, the radial autocorrelation function of electrostatic potential fluctuations ($\widetilde{\phi} = \phi - \phi_{n=0}$) is calculated. The following definition is employed for the autocorrelation function [47]:

$$C(\Delta t, \Delta r) = \frac{\int \mathrm{d}t \int \mathrm{d}r \langle \widetilde{\phi}(t+\Delta t, r+\Delta r, \varphi+\Delta\varphi, \theta=0)\,\widetilde{\phi}(t,r,\varphi,\theta=0)\rangle_\varphi}{\int \mathrm{d}t \int \mathrm{d}r \langle \widetilde{\phi}^2(t,r,\varphi,\theta=0)\rangle_\varphi}, \quad (10)$$

where $\langle\rangle_\varphi$ represents the average in toroidal angle φ. The correlation length is calculated as the full width at the half maximum of $C(\Delta t, \Delta r)$ taking the time average over a time interval $t(\Omega_{ci}^{-1}) = 1.0 \times 10^5 - 2.0 \times 10^5$. It can be seen from figure 9(*a*), both cases (circular and shaped) show the quite similar radial correlation lengths $\Delta r/\rho_s \sim 3.9$ and $\Delta r/\rho_s \sim 3.6$ respectively. Therefore, the eddies size are almost similar in both cases. The plot of probability density functions (PDFs) of the fluxes associated to figure 4(*b*) are shown in figure 9(*b*). From the figure 9(*b*), we see that both cases (circular and shaped) show normal (Gaussian) PDFs and the shapes (and thus moments) of the flux PDFs are close to identical. ZFs are known to play a significant role in the self-regulation of turbulence in tokamaks [44, 48], and they remain undamped in collisionless plasmas [49]. However, as reported in [50–52], ZFs are damped by ion-ion collisions, indicating that collisionality can influence overall turbulence and transport. It would be interesting to perform simulations including collisions and make a qualitative and quantitative comparison of turbulent fluxes, in cases without and with collisions.

4. Linear collisionless electrostatic simulation studies of ITG coupled with kinetic electrons

In this section, linear collisionless electrostatic simulations with kinetic ions and electrons for circular and shaped equilibria are presented. Here, we use the MHD equilibrium code CHEASE [28] to describe the equilibrium. The drift-kinetic electron model is used to treat trapped and passing electrons. The profiles that are considered in these simulation are identical to that used for the adiabatic electron studies reported in the previous sections. The 3D grid resolution used here is $N_s \times N_{\theta_\star} \times N_\varphi = 448 \times 1024 \times 512$. The time step is $\Delta t = 1.0\Omega_{ci}^{-1}$, and the number of markers is $N_p = 200 \times 10^6$. Figures 10(*a*) and (*b*) show the toroidal mode number n scans with kinetic electrons for circular ($\kappa = 1.0$) and shaped ($\kappa = 1.2$ & $\kappa = 1.4$) cases. Both shaped cases have a triangularity $\delta = 0.45$. The inclusion of kinetic electrons strongly enhances the ITG growth rate. The enhancement of ITG growth rate in the presence of fully kinetic electrons is explained as follows. The assumption of an adiabatic response for passing electrons rests on the premise that these particles possess sufficient mobility along magnetic field lines to maintain thermal equilibrium despite field fluctuations. This adiabatic response holds as long as $|\omega_r/k_\parallel| \ll v_{\mathrm{the}}$, wherein the parallel phase velocity $\omega_r/k_\parallel$ of ITG/TEM microinstabilities remains small compared to the electron thermal velocity $v_{\mathrm{the}} = \sqrt{T_{e0}/m_e}$. Here, $k_\parallel$ denotes the component parallel to the magnetic field of a given mode wave vector k, T_{e0} represents the equilibrium temperature of electrons, and m_e stands for their mass. However, in proximity to mode rational surfaces (MRSs) of low order-magnetic surfaces where the safety factor q_s is a low-order rational number ($q_s = -m/n$ with m and n integers)-the validity of the adiabatic assumption becomes questionable. Near such MRSs, resonant Fourier modes with poloidal and toroidal mode numbers (m, n) align with magnetic field lines, yielding $k_\parallel \approx (nq_s + m)/Rq_s = 0$. Consequently, the associated parallel phase velocity $\omega_r/k_\parallel$ surpasses the electron thermal velocity v_{the} within a radial range δx around this surface [34, 53–56]. This violation of the adiabatic response condition becomes apparent within

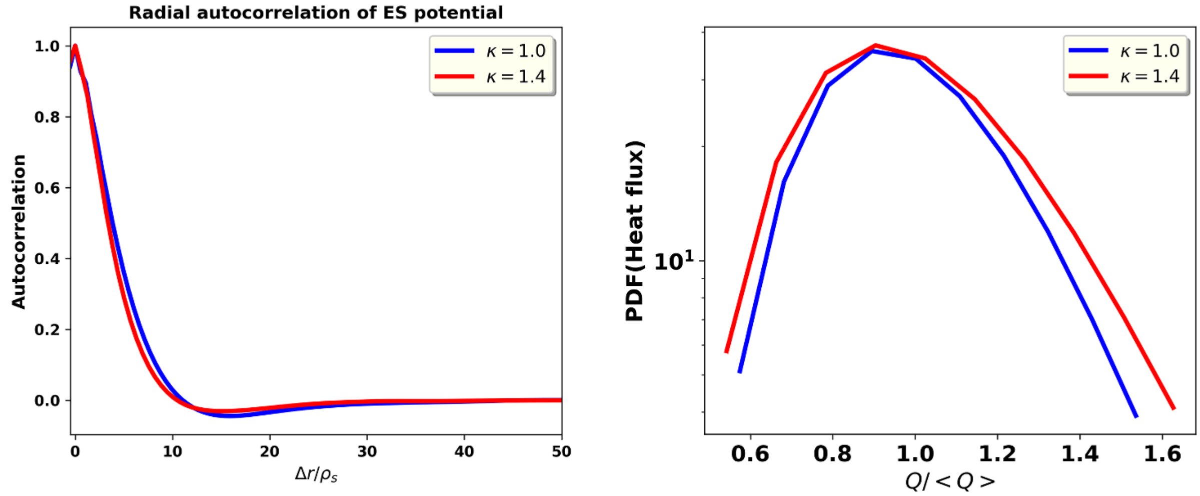

Figure 9. (*a*) Radial autocorrelation functions computed from fluctuating electrostatic potential for circular and shaped ($\kappa = 1.4$ cases, during the time period of $t(\Omega_{ci}^{-1}) = 1.0 \times 10^5 - 2.0 \times 10^5$ and (*b*) The probability density function (PDF) of the heat flux for circular and shaped ($\kappa = 1.4$) cases.

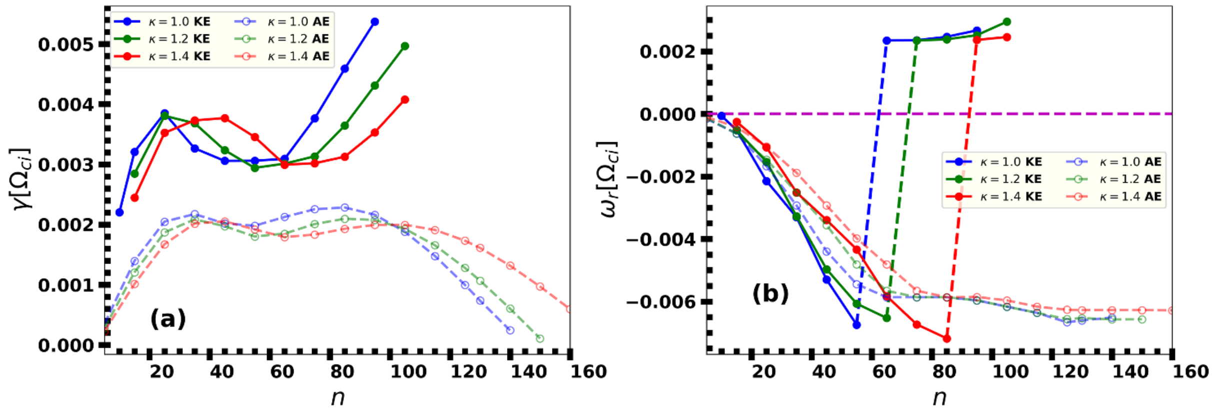

Figure 10. (*a*) Growth rate (γ) and (*b*) Real frequency (ω_r) plots for circular ($\kappa = 1.0$) and shaped ($\kappa = 1.2$ & $\kappa = 1.4$) magnetic equilibria for adiabatic electron (AE) and kinetic electron (KE) cases. The AE cases (also figure 2) are shown with open circles and dashed lines for comparison.

this interval. When incorporating the fully kinetic response of electrons, fine structures emerge in eigenmode configurations near MRSs due to their non-adiabatic behavior. The destabilization phenomena near MRSs associated with passing electron dynamics have been elucidated through a local dispersion relation [54]. It has been observed that within the radial domain where fine structures linked to the non-adiabatic response of passing electrons manifest, the growth rate predicted by the local dispersion relation markedly increases, often by a factor of two or more, upon accounting for the non-adiabatic electron response [24, 34, 53–55, 57, 58]. The increase in the growth rate of the ITG mode due to the presence of trapped electrons can be explained as follows. In a toroidal plasma, a pressure perturbation on the outboard side creates localized regions of higher and lower temperatures. The magnetic drift velocity of ions, which depends on temperature, varies in these regions, causing fluctuations in local ion density. This results in a potential perturbation and results in a corresponding poloidal electric field. This electric field, in combination with the applied magnetic field, drives plasma particles radially due to the $E \times B$ drift. When electrons are considered adiabatic, the moment charge separation is produced, adiabatic electrons neutralize the space charge, preventing or reducing the buildup of $E \times B$ advection. However, in a toroidal geometry, the $1/R$ dependence of magnetic field, results in some electrons being 'trapped' in regions of weaker magnetic field. These trapped electrons cannot respond adiabatically to neutralize the charge separation, allowing the mode to grow for a finite time [18, 59]. Therefore, the ITG growth rate increases in the presence of trapped electrons. In a high n region, the ITG mode is stabilized by the finite Larmor radius (FLR) effect, and dominant. This is likely the TEM, but a proper treatment of collisions, for example, is necessary to characterize the mode. In the ADITYA-U experimental shot under investigation, the normalized electron and ion collisionality defined as the ratio between the detrapping collision frequency and the bounce frequency [60–62] ($\nu^*_{i,e} = \frac{qR_0}{\epsilon^{3/2}\tau_{ii,ei}v_{Ti,e}}$), $\nu^*_i \sim 2.5$ & $\nu^*_e \sim 3.4$, $\nu^* \sim 2.5 - 3.4$. Here, q is the safety factor, R_0 is the major radius, ϵ is the local inverse aspect ratio, v_{Te} and v_{T_i} are the electron and ion thermal velocity τ_{ii} is the ion-ion

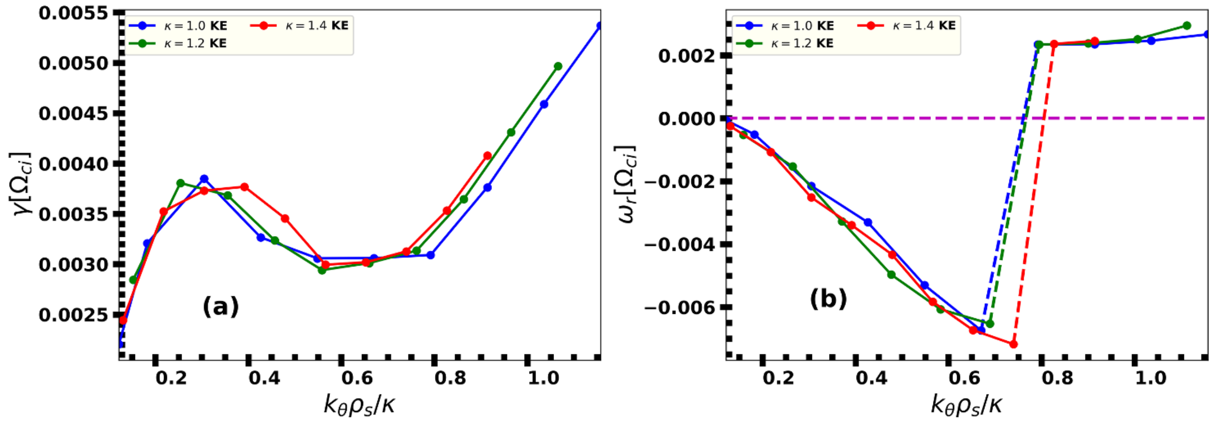

Figure 11. (*a*) Growth rate (γ) and (*b*) Real frequency (ω_r) plots for circular ($\kappa = 1.0$) and shaped ($\kappa = 1.2$ & $\kappa = 1.4$) magnetic equilibria for kinetic electron (KE) cases as a function of the effective poloidal wave number $k_\theta\rho_s/\kappa$.

collision time and τ_{ei} is the electron-ion collision time. At such high values of collisionality ($\nu^* \gg 1$), it is likely that the TEM will be suppressed in more complete gyrokinetic simulations with collisions included [14, 15, 63]. Therefore, we speculate that at high toroidal wavenumbers, the ETG may be the relevant mode. For our present parameters and profiles, we believe that these modes are not ETG. In order to verify that the high n modes are indeed TEM, separate simulations are conducted (not shown here) using the hybrid electron model, that contains the effect of trapped electrons only. If these modes were ETG, the growth rates of the high n modes, calculated from the hybrid electron model are expected to very weak. However, on the contrary, we observe strong growth rates at high n modes. This corroborates that the high n modes are TEM. Therefore, in the limit of the current simulations with no collisions and ion-scale wavenumbers, the mode propagating in the electron diamagnetic direction is the TEM. Both figures 10(*a*) and (*b*) illustrate alterations not only in frequency and growth rate values but also in the transition trends from ITG to Trapped Electron Mode (TEM), which vary with different elongations. In the scan of elongation parameter κ, higher κ values stabilize TEMs by reducing the effective temperature gradient across the magnetic flux surface. The global ITG-TEM mode experiences an effective temperature gradient, which is reduced due to the extension of plasma shape in the vertical direction. This modification is expressed as $\frac{R(1-E')}{L_T}$, where $E' = r(\kappa-1)/(\kappa+1)$ and r denotes the magnetic surface label coordinate [25]. These findings are consistent with prior literature discussing the global impact of elongation on ITG/TEM through gyro-kinetic simulations [23–25]. A higher elongation leads to a decrease in frequency and an increase in the transition toroidal wave number n, marking the point where the ITG mode transitions to TEM. Examining the growth rate, figure 10(*a*) reveals that as elongations increase, the highest growth rate of the ITG branch is weakly affected. Simultaneously, the overall spectrum widens, with the maximum growth rate shifting to higher n (smaller scales) [23, 24]. This observation aligns with the previously discussed elongation effect on the ITG mode with adiabatic electrons in section 3.1.

The influence of elongation is also explained through the concept of 'effective poloidal wavenumber' (where elongation causes a contraction in poloidal wavelength by a factor of $1/\kappa$ on the low field side) [23, 24]. In a simplified case with zero triangularity and no Shafranov shift, the relationship between the effective poloidal wavenumber k'_θ and the conventional one k_θ can be expressed as $k'_\theta \sim k_\theta/\kappa$, derived from analytical equilibrium [23]. When the growth rates are replotted with respect to the effective poloidal wavenumber k_θ/κ, as depicted in figure 11, the three cases exhibit good agreement.

The top panel (kinetic circular equilibrium) of figure 12 shows 2D poloidal mode structures of electrostatic potential in the (R,Z) plane. In the enlarged view of the $n = 95$ and $n = 105$ modes, we can see a signature of two distinct structures. It is likely that the ITG and TEM instability co-exists, but we expect that with time only the dominant mode survives. As depicted in bottom panel of figure 12(*d*) for toroidal mode number $n = 105$, the presence of non-adiabatic passing electrons results in the emergence of shorter scales in the mode structures. These electrons near the $k_\parallel = 0$ surfaces, are unable to suppress charge separation by following the field lines. Consequently, at these surfaces, the charge separation leads to a more pronounced $E \times B$ drift and heightened instability [18]. As a result, the linear mode structure undergoes a breakdown into shorter length scales.

5. Summary

Effects of magnetic equilibrium shaping (elongation and triangularity) have been performed on ITG-SWITG modes in ADITYA-U tokamak. From the linear results, we see that growth rate and real frequency are reduced with magnetic shaping and growth rate is shifted towards higher toroidal wave number. From the nonlinear results, we see that heat flux is reduced a little with magnetic shaping as compared to circular case. Linear collisionless electrostatic simulation studies of ITG coupled with kinetic electrons have also been performed. The results indicate that growth rate and real frequency of the ITG mode are significantly increased in the presence of kinetic

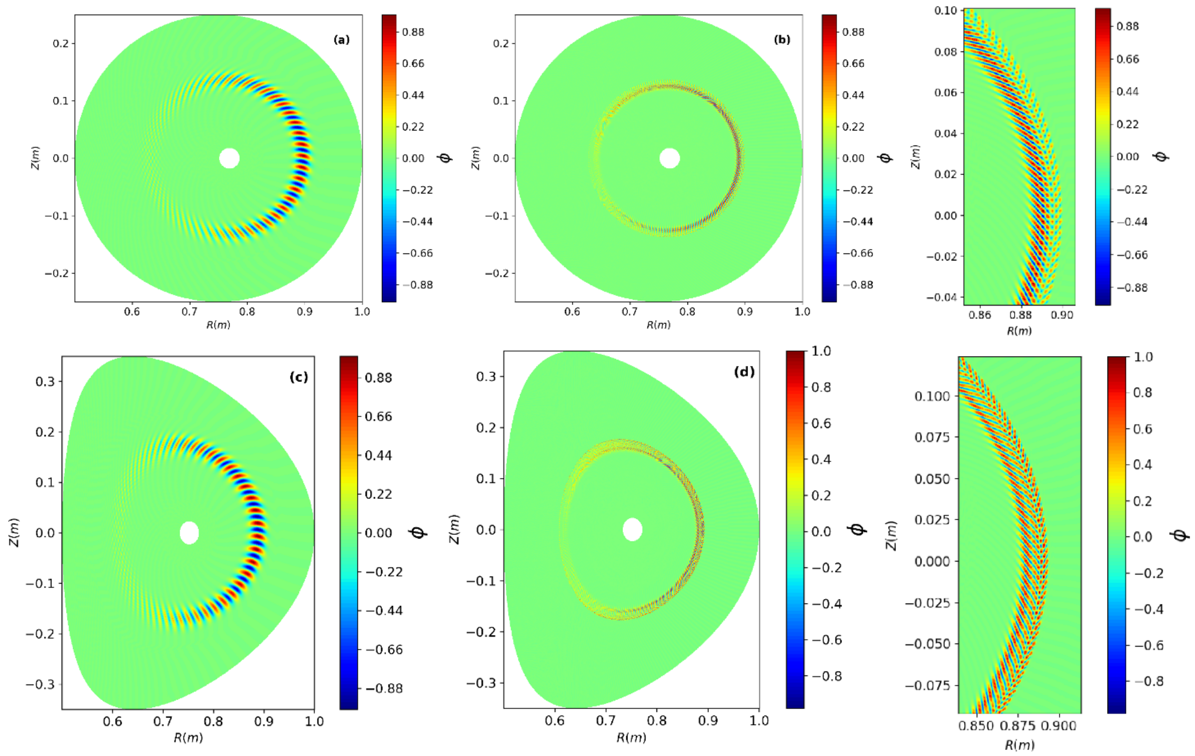

Figure 12. The top panel shows poloidal mode structures of the electrostatic potential in the (R, Z) plane for kinetic electron simulations for the circular equilibrium, from left to right, toroidal mode numbers (a) $n = 25$ & (b) $n = 95$ and a zoomed-in image of the $n = 95$ mode. Bottom panel shows the mode structures of the electrostatic potential in the (R, Z) plane for kinetic electron simulations for the shaped equilibrium ($\kappa = 1.4$), from left to right, toroidal mode numbers (c) $n = 25$ & (d) $n = 105$ and a zoomed-in image of the $n = 105$ mode. All the mode structures are plotted here at the final time of simulation.

electrons. At higher toroidal mode numbers, a mode is found to be propagating in the electron diamagnetic direction. This is the TEM, but a proper treatment of collisions, for example, is necessary to characterize the mode in ADITYA-U. Robust nonlinear simulations with kinetic electrons is resource intensive ($\sim 10^6$ CPU-hours per simulation) and our future work therefore aims to first understand the importance of collisions and electromagnetic effects. Collisions will impact trapped particles and therefore any TEM-like mode, whereas the inclusion of finite β could strongly impact the ITG through β' stabilization. Another approach may be to quantify the importance of global effects by comparing against flux tube codes (such as GENE, GKW) for the well understood adiabatic electron case and utilizing these far less computationally demanding tools for more complete kinetic studies. It is important to note that, the collisions can reduce the magnitude of ZF which can enhance the ITG turbulence, and hence transport level. Also, with fully kinetic electron model, study of ETG mode at higher toroidal mode numbers is an interesting study. We aim to carry out simulations along this line in future publications.

Acknowledgments

The authors are grateful to the ADITYA-U operations and diagnostics team for providing the experimental data. The simulations reported here were in part performed using IPR's HPC facility ANTYA. A. Bokshi would like to acknowledge funding through UKRI Grants EP/R034737/1 and EP/X035336/1, allowing time and access to the ARCHER2 UK National Supercomputing Service (www.archer2.ac.uk).

ORCID iDs

Amit K. Singh https://orcid.org/0000-0001-8350-9459
A. Bokshi https://orcid.org/0000-0001-7095-7172
R. Ganesh https://orcid.org/0000-0002-5095-3067
T. Hayward-Schneider https://orcid.org/0000-0003-0588-5090
A. Mishchenko https://orcid.org/0000-0003-1436-4502
L. Villard https://orcid.org/0000-0003-3807-9482

References

[1] Rewoldt G. and Tang W.M. 1990 *Phys. Fluids* B **2** 318–23
[2] Lang J., Parker S.E. and Chen Y. 2008 *Phys. Plasmas* **15** 055907
[3] Merz F. and Jenko F. 2010 *Nucl. Fusion* **50** 054005
[4] Smolyakov A.I., Yagi M. and Kishimoto Y. 2002 *Phys. Rev. Lett.* **89** 125005
[5] Gao Z., Sanuki H., Itoh K. and Dong J.Q. 2003 *Phys. Plasmas* **10** 2831
[6] Chowdhury J. *et al* 2012 *Phys. Plasmas* **19** 102508

[7] Mishchenko A. *et al* 2006 *AIP Conf. Proc.* **871** 394–9
[8] Merlo G. *et al* 2018 *Plasma Phys. Control. Fusion* **60** 034003
[9] Tanna R.L. *et al* 2019 *Nucl. Fusion* **59** 112006
[10] Tanna R.L. *et al* 2022 *Nucl. Fusion* **62** 042017
[11] Singh A.K. *et al* 2023 *Nucl. Fusion* **63** 086029
[12] Jolliet S., Bottino A., Angelino P., Hatzky R., Tran T.M., Mcmillan B.F., Sauter O., Appert K., Idomura Y. and Villard L. 2007 *Comput. Phys. Commun.* **177** 409–25
[13] Lanti E. *et al* 2020 *Comput. Phys. Commun.* **251** 107072
[14] Vernay T., Brunner S., Villard L., McMillan B.F., Jolliet S., Bottino A., Görler T. and Jenko F. 2013 *Plasma Phys. Control. Fusion* **55** 074016
[15] Kwon J.-M., Qi L., Yi S. and Hahm T.S. 2017 *Comput. Phys. Commun.* **215** 81–90
[16] Rewoldt G., Lin Z. and Idomura Y. 2007 *Comput. Phys. Commun.* **177** 775–80
[17] Singh T. *et al* 2023 *Nucl. Fusion* **63** 056008
[18] Chowdhury J., Ganesh R., Brunner S., Vaclavik J., Villard L. and Angelino P. 2009 *Phys. Plasmas* **16** 052507
[19] Zhang N., Gong X.Y., Dong J.Q., Huang Q.H., Gong L. and Li J.C. 2016 *Phys. Plasmas* **23** 042508
[20] Chowdhury J., Ganesh R., Vaclavik J., Brunner S., Villard L. and Angelino P. 2009 *Phys. Plasmas* **16** 082511
[21] Kinsey J.E., Waltz R.E. and Candy J. 2007 *Phys. Plasmas* **14** 102306
[22] Belli E.A., Hammett G.W. and Dorland W. 2008 *Phys. Plasmas* **15** 092303
[23] Lei P., Kun H., Qiaogen Z. and Chunliang L. 2016 *Phys. Plasmas* **23** 062513
[24] Wang W., Imadera K., Seto H. and Yagi M. 2022 *Nucl. Fusion* **62** 112006
[25] Angelino P. *et al* 2009 *Phys. Rev. Lett.* **102** 195002
[26] Candy J. and Waltz R.E. 2003 *Phys. Rev. Lett.* **91** 045001
[27] Lapillonne X., Brunner S., Dannert T., Jolliet S., Marinoni A., Villard L., Görler T., Jenko F. and Merz F. 2009 *Phys. Plasmas* **16** 032308
[28] Lütjens H., Bondeson A. and Sauter O. 1996 *Comput. Phys. Commun.* **97** 219
[29] Bottino A., Vernay T., Scott B., Brunner S., Hatzky R., Jolliet S., McMillan B.F., Tran T.M. and Villard L. 2011 *Plasma Phys. Control. Fusion* **53** 124027
[30] Vernay T., Brunner S., Villard L., McMillan B.F., Jolliet S., Tran T.M. and Bottino A. 2012 *Phys. Plasmas* **19** 042301
[31] Singh A.K. *et al* 2023 *29th IAEA Fusion Energy Conf. (FEC 2023)* (*London, United Kingdom, 16–21 October 2023*) (available at: https://conferences.iaea.org/event/316/papers/28193/files/10864-FEC_2023_preprint_Amit_Singh.pdf)
[32] Hirose A., Elia M., Smolyakov A.I. and Yagi M. 2002 *Phys. Plasmas* **9** 1659
[33] Gao Z., Sanuki H., Itoh K. and Dong J.Q. 2005 *Phys. Plasmas* **12** 022502–1
[34] Dominski J., McMillan B.F., Brunner S., Merlo G., Tran T.-M. and Villard L. 2017 *Phys. Plasmas* **24** 022308
[35] Mishchenko A., Könies A. and Hatzky R. 2005 *Phys. Plasmas* **12** 062305
[36] Mishchenko A., Hatzky R., Sonnendrücker E., Kleiber R. and Könies A. 2019 *J. Plasma Phys.* **85** 905850116
[37] McMillan B.F., Jolliet S., Tran T.M., Villard L., Bottino A. and Angelino P. 2008 *Phys. Plasmas* **15** 052308
[38] Villard L., Angelino P., Bottino A., Brunner S., Jolliet S., McMillan B.F., Tran T.M. and Vernay T. 2013 *Plasma Phys. Control. Fusion* **55** 074017
[39] Villard L. *et al* 2019 *Plasma Phys. Control. Fusion* **61** 034003
[40] Di Giannatale G. *et al* 2024 *Plasma Phys. Control. Fusion* **66** 095003
[41] Tran T.M., Appert K., Fivaz M., Jost G., Vaclavik J. and Villard L. 1999 *Proc. Joint Varenna - Lausanne Int. Workshop on Theory of Fusion Plasmas (Bologna Editrice Compositori, Societa Italiana di Fisica)* (*Varenna, Italy, 31 August –4 September 1998*) ISPP-18 pp 45–58 (available at: https://infoscience.epfl.ch/handle/20.500.14299/24834)
[42] Bourdelle C., Hoang G.T., Litaudon X., Roach C.M. and Tala T. (Physics, for the ITPA Topical Group on Trans., Group, the International ITB Database Work) 2005 *Nucl. Fusion* **45** 110
[43] Anderson J., Nordman H. and Weiland J. 2000 *Plasma Phys. Control. Fusion* **42** 545
[44] Rogers B.N. *et al* 2000 *Phys. Rev. Lett.* **85** 5336
[45] Diamond P.H., Itoh S.-I., Itoh K. and Hahm T.S. 2005 *Plasma Phys. Control. Fusion* **47** R35
[46] Xiao Y. and Catto P.J. 2006 *Phys. Plasmas* **13** 082307
[47] Asahi Y., Grandgirard V., Idomura Y., Garbet X., Latu G., Sarazin Y., Dif-Pradalier G., Donnel P. and Ehrlacher C. 2017 *Phys. Plasmas* **24** 102515
[48] Lin Z., Hahm T.S., Lee W.W., Tang W.M. and White R.B. 1998 *Science* **281** 1835
[49] Rosenbluth M.N. and Hinton F.L. 1998 *Phys. Rev. Lett.* **80** 724
[50] Lin Z., Hahm T.S., Lee W.W., Tang W.M. and Diamond P.H. 1999 *Phys. Rev. Lett.* **83** 3645
[51] Falchetto G., Ottaviani M. 2004 *Phys. Rev. Lett.* **92** 025002
[52] Dif-Pradalier G., Grandgirard V., Sarazin Y., Garbet X. and Ghendrih P. 2009 *Phys. Rev. Lett.* **103** 065002
[53] Chowdhury J., Ganesh R., Angelino P., Vaclavik J., Villard L. and Brunner S. 2008 *Phys. Plasmas* **15** 072117
[54] Dominski J., Brunner S., Görler T., Jenko F., Told D. and Villard L. 2015 *Phys. Plasmas* **22** 062303
[55] Dominski J. *et al* 2012 *J. Phys.: Conf. Ser.* **401** 012006
[56] Ajay C.J., Brunner S., McMillan B., Ball J., Dominski J. and Merlo G. 2020 *J. Plasma Phys.* **86** 905860504
[57] Chen Y., Parker S.E., Cohen B.I., Dimits A.M., Nevins W.M., Shumaker D., Decyk V.K. and Leboeuf J.N. 2003 *Nucl. Fusion* **43** 1121
[58] Heikkinen J.A., Janhunen S.J., Kiviniemi T.P. and Ogando F. 2008 *J. Comput. Phys.* **227** 5582
[59] Redd A.J., Kritz A.H., Bateman G., Rewoldt G. and Tang W.M. 1999 *Phys. Plasmas* **6** 1162–7
[60] Vernay T., Brunner S., Villard L., McMillan B.F., Jolliet S., Tran T.M., Bottino A. and Graves J.P. 2010 *Phys. Plasmas* **17** 122301
[61] Dif-Pradalier G. *et al* 2011 *Phys. Plasmas* **18** 062309
[62] Idomura Y. 2016 *J. Comput. Phys.* **313** 511–31
[63] Ryter F., Angioni C., Peeters A.G., Leuterer F., Fahrbach H.-U. and Suttrop W. 2005 *Phys. Rev. Lett.* **95** 085001